Initial interpretation of Laser-induced Incandescence (LII) signals from flame-generated TiO2 particles: Towards a quantitative characterization of the flame synthesis processes

J. Yi, Christopher Betrancourt, N. Darabiha, B. Franzelli

Graphical Abstract

Initial interpretation of Laser-induced Incandescence (LII) signals from flame-generated TiO_2 particles: towards a quantitative characterization of the flame synthesis processes ⋆

J. Yi, C. Betrancourt, N. Darabiha, B. Franzelli

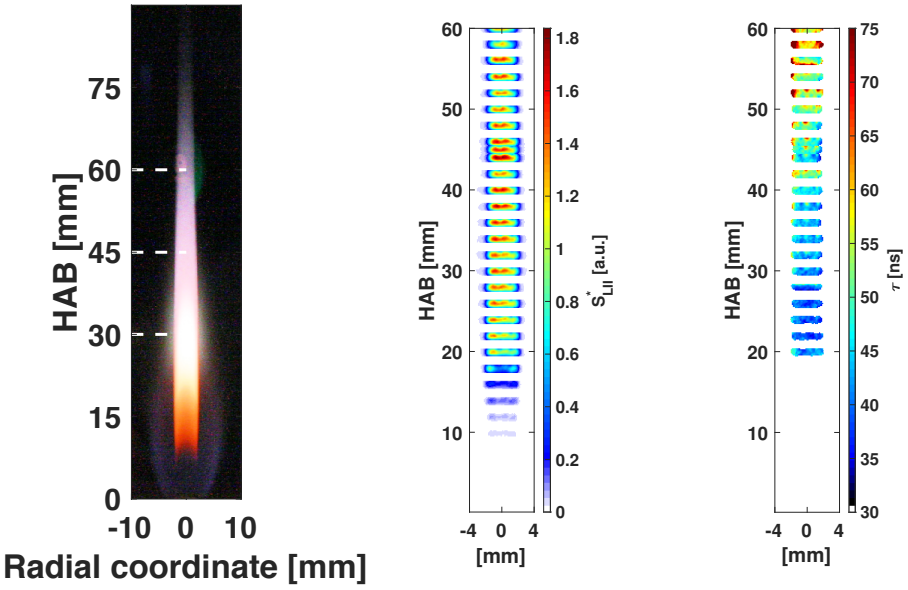

Initial interpretation of Laser-induced Incandescence (LII) signals from flame-generated TiO_2 particles: towards a quantitative characterization of the flame synthesis processes

J. Yi[a], C. Betrancourt[a], N. Darabiha[a], B. Franzelli[a,*]

[a]*Laboratoire EM2C, CNRS, CentraleSupélec, Université Paris-Saclay, Gif-sur-Yvette, 91190, France*

Abstract

Among various optical diagnostics for the characterization of particle formation in flames, laser-induced incandescence (LII), developed for soot particles, is attracting attention for the study of flame synthesis of metal-oxides. Among them, TiO_2 nanoparticles are widely used for pigments and photocatalysts. Recent works have shown the feasibility of LII for flame-synthesized TiO_2, but extensive research is still needed to quantitatively characterize TiO_2 production in flames with LII measurements. In this work, the first attempt towards the characterization of TiO_2 synthesis in flames is provided as a normalized volume fraction. To achieve this, TiO_2 nanoparticles are generated in a laminar coflow diffusion flame of argon-diluted hydrogen and air with pre-vaporized titanium isopropoxide (TTIP). A 355 nm laser is used to irradiate the flame-generated particles. Spectral, temporal, and spatial measurements are performed at various flame heights. First, laser-induced emission (LIE) at prompt is investigated for different laser fluences to identify the operating conditions that ensure the LII-like nature of the measured signals. The LIE at high fluence presents sharp features that contain information on the atomic composition of the particles and of the vaporized species when compared to reference spectra of carbon black and high-purity

*This document is the results of the research project funded by the European Research Council (ERC).

*Corresponding author

Email address: benedetta.franzelli@centralesupelec.fr (B. Franzelli)

TiO_2 particles. Then, the LII signal at lower fluence is used to obtain an estimation of the spatial evolution of the normalized volume fraction and of the LII signal decay time. These results are finally used to discuss the major aerosol processes along the flame centerline.

Keywords: flame synthesis, titanium dioxide TiO_2, Laser-induced incandescence (LII), LII decay time, volume fraction

---

Introduction

Nanoparticle synthesis via flame spray pyrolysis has gained significant interest due to its efficiency and versatility in producing high-quality particles with tailored properties [1]. To achieve good control of the characteristics of the produced nanoparticles, a deep understanding of the processes governing nanoparticle production in the flame is required. Thus, in-situ diagnostics are increasingly used to investigate the spatial evolution of the characteristics of metal-oxides along the flame [2]. Specifically to TiO_2, Ren et al. [3] provided instantaneous two-dimensional imaging of TiO_2 nanoparticle formation in turbulent jet diffusion flame through a phase-selective laser-induced breakdown spectroscopy (PS-LIBS) technique. Franzelli et al. [4] investigated the spatial description of TiO_2 nanoparticle synthesis in a turbulent isopropyl alcohol flame by multiple diagnostics including shadowgraphy and light scattering. Finally, laser-induced incandescence (LII) technique, originally developed for the study of the formation of carbonaceous particles in flames [5], has also been applied to various non-soot nanoparticles [6] including TiO_2 [7, 8, 9, 10, 11]. However, to the best of our knowledge, this technique has yet to be used to obtain quantitative two-dimensional fields of volume fraction f_v and primary particle diameter d_pp of TiO_2 nanoparticles in flames. This is probably due to the challenge of interpreting the LII signal. The two causes of this challenge are:

- Laser-induced emission (LIE) can be characterized not only by thermal LII signal but also by non-thermal emissions such as laser-induced fluorescence (LIF) [9] and/or phase-selective laser-induced breakdown spectroscopy (PS-LIBS) [12].

- Experimental data on TiO_2 optical properties, specifically the refractive index absorption function $E(m_\lambda)$, present large variability and uncertainties [13, 14], affecting the LII signal interpretation.

The objective of this study is to provide indications on the interpretation of the LII signal in terms of the normalized volume fraction f_v^* of TiO_2 nanoparticles in flame synthesis. Combined with information on the LII signal decay time τ, f_v^* results will lead to a first insight into the aerosol physical processes governing TiO_2 production along a laminar coflow diffusion H_2/Ar/TTIP flame.

This article is organized as follows: first, the experimental set-up is described in Sec. 1. Next, LIE of flame-synthesized TiO_2 nanoparticles is characterized in Sec. 2. Then, section 3 introduces the spatial evolution of the LII signal as well as its temporal decay τ. Finally, information on the normalized volume fraction f_v^* and on τ along the flame centerline are used to discuss aerosol processes.

1. Experimental set-up

The experimental set-up used in this work is illustrated in Fig. 1 and is constituted by three parts: the laser heating, the signal detection, and a laminar coflow flame for the synthesis of TiO_2 particles. The system has already been used in [11], where the LII feasibility for high purity TiO_2 nanoparticles has been proven. The system is briefly described in the following. Additional details can be found in [11].

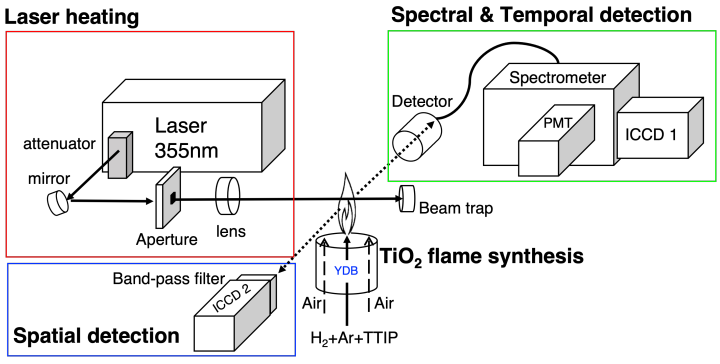

Figure 1: Schematic representation of the experimental set-up developed to investigate TiO_2 nanoparticle synthesis in flame via LII.

1.1. Laser heating

The heating system accounts for an Nd:YAG laser (Quantel,Q-smart 850, 355 nm) with an FWHM 5 ns width pulse working at 10 Hz. The laser fluence

is adjusted through an attenuator that consists of a half-wave plate and two polarizers. A beam profiler (Gentec Beamage) is employed to monitor the energy distribution of the nearly top-hat-shaped laser, which is 1:1 relay-imaged at the centerline of the burner.

1.2. Diffusion coflow flame

To synthesize TiO_2 nanoparticles in flame, the design of the Yale diffusion burner (YDB) [15] is used. The burner consists of a central fuel tube (inner diameter D_i= 3.9 mm) surrounded by air coflow (inner diameter D_o = 76 mm). The precursor used to generate TiO_2 nanoparticles is titanium isopropoxide $Ti(OCH(CH_3)_2)_4$ (TTIP, Sigma Aldrich, purity $\geq$ 97.0%) stored in a pressurized bottle at 6 bar with a N_2. The TTIP mass flow rate is controlled by a Coriolis flowmeter (Bronkhorst, MINI CORI-FLOW, ML120V21-BAD-11-0-S). It is introduced through a heated line at 403 K to ensure its vaporization. The TTIP vapor is then mixed with H_2-Ar mixture heated at 353 K and transported to the thermalized burner at 423 K. Finally, at the exit of the burner, the temperature keeps 380 K for the fuel exit in the middle and around 412 K for the coflow air exit. Temperatures have been measured using K-type thermocouples. A detailed description of the injection and heating system can be found in [11].

H_2 was chosen as the fuel for synthesizing TiO_2 nanoparticles in order to minimize the presence of carbon species. To increase the stability of the flame, the fuel was mixed with Ar in the fuel tube. In order to limit hydrolysis during precursor pre-vaporization, the H_2O levels in hydrogen and argon were strictly controlled to be below 0.5 ppm. The operating conditions are presented in Table 1. The H_2-Air flame without TTIP injection is illustrated in Fig. 2(a). Upon injection of TTIP into the hydrogen flame, a bright, cylindrical area with a diameter of approximately 4.5 mm is observed, as shown in Fig. 2(b). The flame structure is schematically illustrated in Fig. 2(c). The central luminous zone indicates the presence of TiO_2 nanoparticles. This zone changes color from orange to white and then has a pale-blue tail. The bright zone is surrounded by a much weaker luminescent emission indicating the position of the reaction zone, similar to the hydrogen flame without TTIP (Fig. 2(a)).

Fuel				Coflow	
$\dot{m}_{H_2}$	$\dot{m}_{Ar}$	$\dot{m}_{TTIP}$	T_F	$\dot{m}_{air}$	T_C
5.1 g/h	2.3 g/h	0.5 g/h	380 K	7759 g/h	412 K

Table 1: Operating conditions for the preheated hydrogen and precursor (TTIP) coflow flame. The inflow velocity is 1.9 m/s, and the coflow velocity is 0.55 m/s. T_F is the temperature of the fuel exit and T_C is the temperature at the coflow.

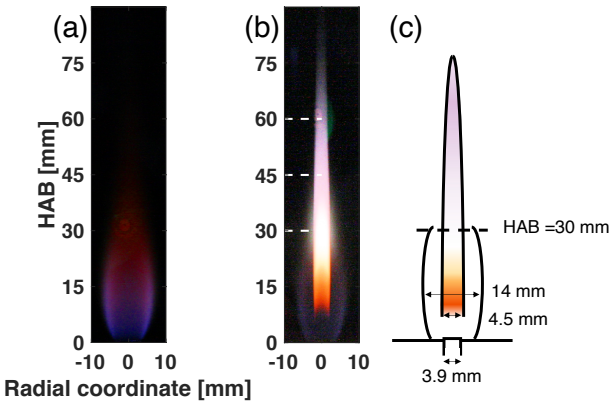

Figure 2: Typical images of the luminosity of H_2/Ar/Air coflow diffusion flames without (a) and with (b) injection of TTIP precursor. The camera exposition is adapted for better visualization for each figure. (c) Schematic illustration of H_2/Ar/Air/TTIP flame.

1.3. Detection systems

Three types of information on the LIE are collected along the flame as schematically illustrated in Fig. 3: spatial, temporal, and spectral characterization. For spectral and temporal measurements, the induced signal is collected at 90° using a telescope composed of two two-inch achromatic lenses ($f_1 = 200$ mm and $f_2 = 100$ mm). Two notch filters (355 and 532 nm) are used to suppress the laser harmonic signal. The collected signal is then focused on a 365 μm multimode optical fiber (Thorlabs, FG365UEC) leading to the entrance slit of a spectrometer resulting in a spectral resolution of 0.17 nm. The signal is imaged at 10 Hz with a gate width of 20 ns at different gate delays using a spectrometer (Princeton Instrument, Spectra Pro HRS-500, f = 500 mm, 150 grooves/mm), which is coupled with an intensified CCD camera or a photomultiplier tube. The intensified CCD camera (ICCD1,

Princeton Instruments, PI-MAX 4 1024EMB) is used to acquire spectral information. The spectral detection system is calibrated using a tungsten filament lamp for signal intensity and a mercury lamp for wavelength. The spectral measurements are conducted only at HAB=30, 45, and 60 mm. The time-resolved LIE signal is measured using a photomultiplier (PMT, HAMAMATSU, R2257) at 640±10 nm and is recorded using an oscilloscope (Lecroy wave surfer 434, 350MHz bandwidth, 2GS/s sampling rate). Temporal measurements have been performed along all the flame heights above 10 mm. Both spectral and temporal measurements are done at the centerline of the flame synthesis. The spectral signal is time-averaged over 5000 single-shot measurements for each position and gate delay. Seven hundred single-shot measurements are averaged for the temporal measurements at each spatial position. At the opposite side of the telescope detector, an intensified camera (ICCD2, Princeton Instruments, PI-MAX 4, 1024i) equipped with a bandpass filter centered at 640 nm ± 7 nm (Edmund optics, 86995) is placed to study the spatial distribution of the LIE. Signals are recorded in a two-dimensional grid with a width of 8 mm and a height of 1 mm, covering the homogeneous laser top-hat with a height of 0.9 mm. The detection timing is synchronized with the laser peak and the detection gate τ_D is delayed at 0, 50, 100, 150, 250 ns. The gate width is 20 ns. The detection wavelength at 640 nm is considered in this study where the non-thermal laser-induced emissions can be avoided during LII measurement of TiO_2, as demonstrated in [11].

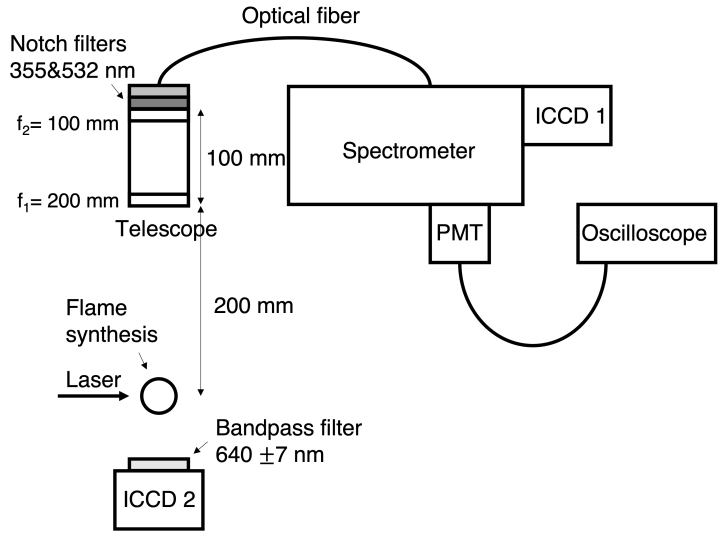

Figure 3: Schematic presentation of the detection system for LII measurement.

Spatial measurements are performed every 2 mm along the flame by moving the burner holder using a hydraulic crank with an accuracy of 10 μm in the z-direction (height above the burner, HAB). 200 single-shot images are averaged for each position. Exemplary data of LII measurements for these three detection systems are provided in Fig. 4. Each (spectral, temporal, spatial) measurement displayed in this work is corrected with the background.

The consistency of the three detection devices and the measurement repeatability are presented in Appendices A and B, respectively.

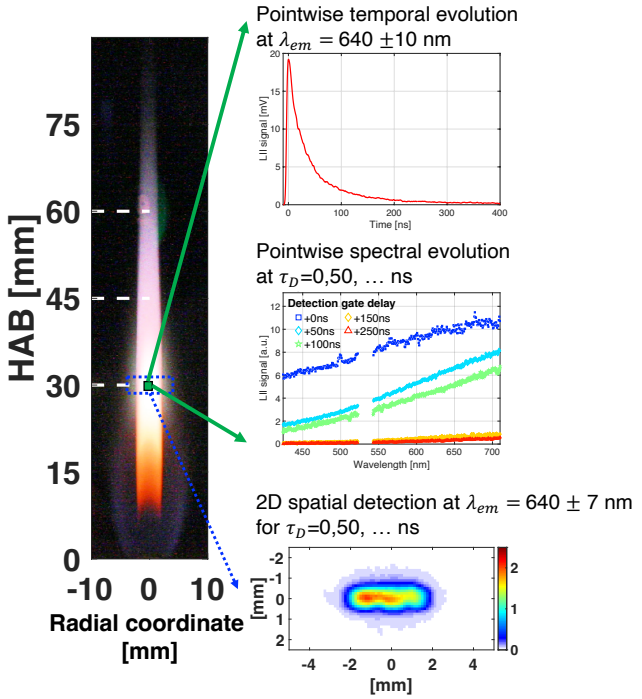

Figure 4: Example illustration of the spatial, temporal, and spectral measurements of LII signal. Positions above HAB=10 mm have been considered for temporal and spatial measurements. Three HABs (HAB=30, 45, 60 mm), localized by the white horizontal lines, have been considered for spectral measurements.

2. Laser-induced emission of flame-synthesized TiO_2

Contrary to carbonaceous particles, metal-oxide nanoparticles can exist in liquid form both before and during the laser interaction due to their lower melting temperature. Liquid-state LII has been investigated in various liquid-state metals and metalloids [16, 17, 18]. The main difficulty is linked to the fact that phase change can cause changes in optical properties. For example, solid silicon is a semiconductor whose absorption spectrum is related to the band-gap energy [19]. On the other hand, liquid silicon behaves like a metal whose optical properties can be described with Drude theory [20]. Liquid silicon has a much higher absorption function than solid state silicon in the visible - IR range [6]. Regarding LII, the higher absorption function in the liquid state can make the particles absorb the laser better, resulting in high temperatures following vaporization. Furthermore, particle morphology

change in a liquid state can raise questions regarding the Rayleigh approximation to interpret the LII signal based on conventional LII theory [21]. To date, no information is available on the optical properties of molten TiO_2 in the literature. Therefore, in the following discussion, solid-state particles are assumed along the flame.

The feasibility of the LII technique for TiO_2 nanoparticles in the burner under scope has already been proven in a previous work [11] using the same experimental set-up. Results of emission spectra at HAB =30 mm for various laser fluences are reported in Fig. 5 to identify the optimal fluence to perform LII measurements. For $F = 0.1$ J/cm^2 and $F = 0.15$ J/cm^2, the signal displays a smooth and broadband emission in the visible range. These features are characteristic of thermal (LII-like) emission. No distinct features are noticed except for the small peak around 500 nm for $F = 0.15$ J/cm^2. However, sharp peaks are noticeable at $F = 0.19$ J/cm^2 and $F = 0.24$ J/cm^2. This suggests that non-thermal interference from LIF and/or PS-LIBS is present, similarly from what has been observed for high-purity TiO_2 nanoparticles in a cold environment [11] or flame-generated TiO_2 nanoparticles excited at 266 nm [22]. Overall, a spectrum shift towards the smallest wavelengths is observed when increasing the laser fluence as classically observed for LII signals [2]. In light of these findings, F= 0.15 J/cm^2 represents a good fluence value to perform LII measurements of flame-synthesized TiO_2, as already reported in our previous work [11]. LIE spectra at this fluence for delayed acquisition times are illustrated in Fig. 6.

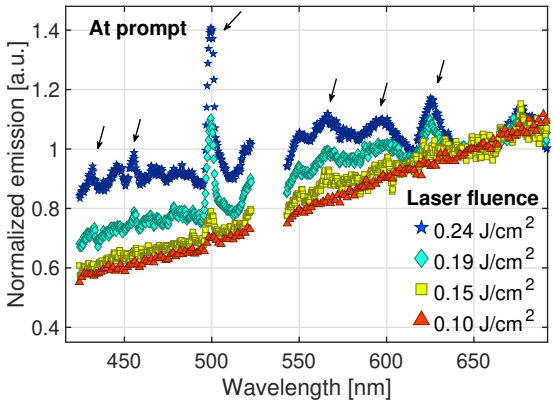

Figure 5: Effect of laser fluence F on prompt LIE spectra for flame-generated TiO_2 nanoparticles at HAB = 30mm. Spectra are normalized by the value of 650 nm. Ti atomic emissions from NIST [23] are represented by arrows.

Results exhibit a red-shift with increasing time delay, indicating a decrease in temperature as predicted by LII theory. As already mentioned from prompt results, there is a peak emission visible at 500 nm that corresponds to Ti emission [23]. These sharp features vanish quickly with time and are not present for longer wavelengths near 640 nm. Therefore, wavelengths longer than 630 nm could be used to perform LII measurements without the need for any delay times for flame-synthesized TiO_2 in the considered flame.

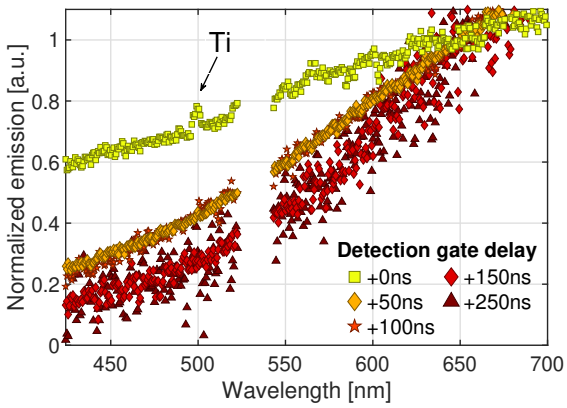

Figure 6: Effect of gate delay (gate width = 20 ns) on emission spectra of LIEs of flame-generated TiO_2 nanoparticles at HAB = 30mm for laser fluence of $F = 0.15$ J/cm^2. Spectra are normalized with the value of the spectrum at 650 nm.

Even if the LII features of the signal have been proven, it is still necessary to verify that the measured LII signal corresponds to TiO_2 nanoparticles and not to carbonaceous materials. As an example, Ren et al. [24] synthesized a carbon-metal-oxide nanocomposite using C_2H_4 in a counterflow burner. In their study, the emission spectrum of carbon-coated TiO_2 nanoparticles showed both the line features from Ti atoms (near 500 nm) and the C_2 emission from the carbonaceous component (near 516 nm), indicating the presence of carbon materials on the surface of TiO_2 particles. Similarly, the C_2 swan bands from the excited carbon species [25] were detected in LIE of TiO_2 nanoparticles synthesized in flames assisted by premixed CH_4/Air flames in the study of De Iuliis et al. [10].

In the present case, if the presence of carbon material was significant enough to contribute to LIE, it would be extremely challenging to discriminate the TiO_2 contribution from the total LII signal, making it impossible to use LII measurements to study the TiO_2 synthesis process. Since TTIP contains carbon molecules, it is necessary to verify if carbon materials may arise from the combustion of TTIP, eventually contributing to the LIE signals in our configurations. For this, the prompt spectrum obtained at the maximum fluence ($F = 0.24$ J/cm^2) is compared in Fig. 7 to reference emission spectra obtained for carbon black and high-purity TiO_2 nanoparticles in a non-reactive particle dispersion system [11]. All spectra exhibit sharp emission features due to excited species of vaporized particles superimposed to a continuous curve. As expected, the emission spectrum of carbon black nanoparticles presents C_2 bands near 468 nm and 516 nm. The emission spectrum of flame-generated TiO_2 nanoparticles in this study does not show any characteristics of these emissions from carbon species. Instead, the emission spectra of flame-generated TiO_2 and high-purity TiO_2 are very similar, indicating that carbon material is likely to be in a negligible proportion in the present configuration. Thus, it can be reasonably presumed that the LII signal originates from TiO_2 nanoparticles. To the best of our knowledge, this is the first time LII is applied to TiO_2 in flames where no carbon traces are detected on LIE at high laser fluence. Still, LIE alone cannot confirm the nature of the investigated particles. Ex-situ measurements such as energy-filtered transmission electron microscopy (TEM) or X-ray diffraction (XRD) will be needed for further confirmation in future works [26].

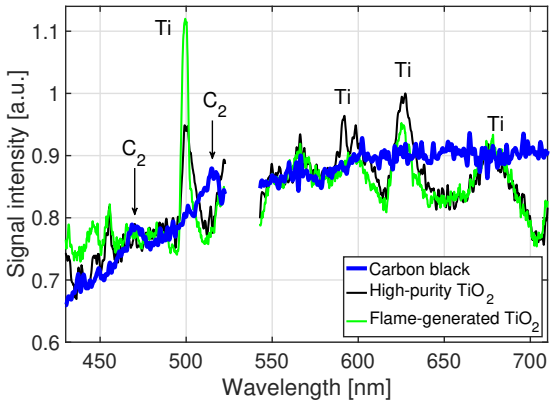

Figure 7: Emission spectra at prompt from carbon black (blue line), high-purity TiO_2 nanoparticle (black line) and H_2 flames-synthesized TiO_2 (at HAB= 30mm) under laser fluence of 0.24 J/cm^2 (green line).

3. Interpretation of LII signal

Once the nature of the emitted signal has been verified to have an LII-like nature and to be originated essentially from TiO_2 particles, it can be analyzed to estimate the volume fraction along the flame. In addition, the signal decay time can be exploited to provide additional information on the spatial evolution of the particle size and/or morphology.

Note that the generated particles are assumed to absorb and emit in the Rayleigh limit [27]. The size parameter criterion ($x = \frac{\pi d_p}{\lambda} << 1$) is satisfied with nano-sized particles and $\lambda_{\text{laser}} = 355$ nm. Still, the phase shift criterion ($x = \frac{\pi d_p}{\lambda} \cdot |m_\lambda| << 1$) requires more attention. For solid TiO_2, it is certainly satisfied due to the small refractive index $|m_\lambda|$ of TiO_2 in the visible range [28]. For liquid TiO_2, however, this is less certain because its refractive index may differ considerably from that of the solid phase. Once again, no studies are available for the optical properties of the molten TiO_2 particles, and the particles are assumed to be in solid states for further analysis in this study.

3.1. Estimation of the normalized volume fraction

The volume fraction f_v can be obtained from the LII signal S_LII at the emission wavelength λ_em from [29]:

$$f_\mathrm{v} = \frac{\eta_\mathrm{CAL} S_{LII}(\lambda_\mathrm{em}, T_\mathrm{eff}) \left[\exp\left(\frac{hc}{\lambda_\mathrm{em} k_B T_\mathrm{eff}}\right) - 1\right]}{\frac{12 E(m_{\lambda_\mathrm{em}}) \pi h c^2}{\lambda_\mathrm{em}^6}} \tag{1}$$

where h is the Planck constant, c is the speed of light in vacuum, and k_B is the Boltzmann constant. T_eff is the effective temperature, representing the weighted average of the particle temperature inside the detection volume. $E(m_\lambda)$ is the absorption function describing the ability of a particle to absorb/emit light at the wavelength λ. η_CAL is a calibration factor that accounts for the effects of laser sheet thickness, detector gain, and other geometrical and spectral factors of the detection system [29].

Thus, to deduce the f_v value from the LII signal, not only the calibration factor η_CAL has to be known, but also the effective temperature T_eff and the $E(m_{\lambda_\mathrm{em}})$ value. Large variability is observed for $E(m_\lambda)$ of TiO_2 nanoparticles in terms of both spectral evolution and values depending on the process used to produce the particles [13, 30, 14, 31]. It is therefore quite challenging to obtain an accurate description of $E(m_\lambda)$ and T_eff for the TiO_2 nanoparticles in the flame. It is however possible to provide a first insight on TiO_2 flame synthesis process by looking at the spatial evolution of the normalized volume fraction f_v^*:

$$\begin{aligned} f_\mathrm{v}^*(z) &= \frac{f_\mathrm{v}(z)}{f_\mathrm{v}(z_0)} \\ &= \frac{S_{LII}(\lambda, z)}{S_{LII}(\lambda, z_0)} \frac{E(m_\lambda, z_0)}{E(m_\lambda, z)} \frac{\left[\exp\left(\frac{hc}{\lambda k_B T_\mathrm{eff}(z)}\right) - 1\right]}{\left[\exp\left(\frac{hc}{\lambda k_B T_\mathrm{eff}(z_0)}\right) - 1\right]} \\ &= \frac{S_{LII}(\lambda, z)}{S_{LII}(\lambda, z_0)} \frac{R(\lambda, z)}{R(\lambda, z_0)} \text{ with } R(\lambda, z) = \frac{\left[\exp\left(\frac{hc}{\lambda k_B T_\mathrm{eff}(z)}\right) - 1\right]}{E(m_\lambda, z)} \end{aligned} \tag{2}$$

where the volume fraction $f_\mathrm{v}(z)$ at position z has been normalized with the volume fraction $f_\mathrm{v}(z_0)$ at position z_0 (here $z_0 = 30$ mm). From Eq. (1), it can be deduced that at a given position z the emission spectra normalized with its value at wavelength λ_em is:

$$\overline{S_{LII}(\lambda, z)} = \frac{S_{LII}(\lambda, z)}{S_{LII}(\lambda_\mathrm{em}, z)} = \frac{R(\lambda_\mathrm{em}, z)}{R(\lambda, z)} \frac{\lambda_\mathrm{em}^6}{\lambda^6} \tag{3}$$

Equation (3) implies that the evolution for the $\overline{S_{LII}(\lambda, z)}$ signal as a function of the wavelength, i.e. its spectral shape, depends on quantity $R(\lambda, z) \cdot \lambda^6$, where only term $R(\lambda, z)$ may vary with z. The normalized emission spectra $\overline{S_{LII}(\lambda, z)}$ at the prompt for TiO_2 nanoparticles at fluence F= 0.15 J/cm^2 at three heights above the burner are presented in Fig. 8. The normalized curves exhibit good superposition. This signifies that the term $R(\lambda, z)$ at a given wavelength λ is constant along the height z. In other words, the shape of the spectral emission is governed by the evolution of $E(m_\lambda)$ as a function of λ and the effective temperature according to Planck's law [32]. Thus, the fact that the shape of the emission spectra does not vary with height indicates that the term:

$$R(\lambda, z) = \left[\exp\left(\frac{hc}{\lambda k_B T_{\text{eff}}(z)}\right) - 1\right] E(m_\lambda, z)^{-1} \tag{4}$$

is constant along the flame centerline. Then, $R(\lambda, z)$ simplifies in Eq. (2). So, the volume fraction along the flame centerline is directly proportional to the LII signal

$$f_{\text{v}}^*(z) = S_{LII}^*(z) = \frac{S_{LII}(\lambda_{\text{em}}, T_{\text{eff}}(z))}{S_{LII}(\lambda_{\text{em}}, T_{\text{eff}}(z_0))}, \tag{5}$$

where $S_{LII}^*(z)$ is the LII signal at position z normalized for its value at $z = z_0$.

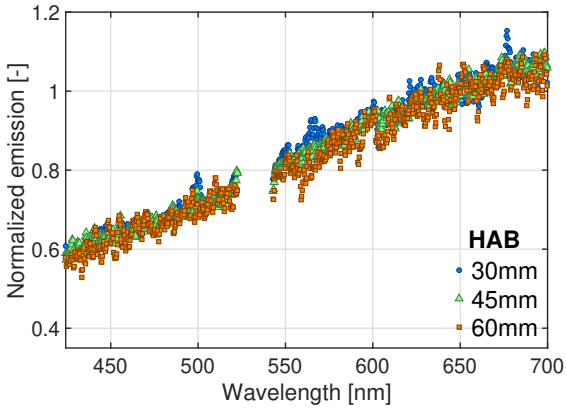

Figure 8: Normalized emission spectra of flame-synthesized TiO_2 at different flame heights under laser fluence $F = 0.15$ J/cm^2. All spectra are normalized to their values at 650 nm. Their superposition indicates that $R(\lambda, z)$ is constant along the flame centerline.

The experimental 2-D spatial distribution of $S_{LII}^*(z)$ is shown in Fig. 9 by considering the LII signal at the prompt. The laser light arrives from the

left side of the image. This explains the signal attenuation from the left to the right side of the image. For HAB < 18 mm, the normalized LII signal is localized at the flame wings. For higher HABs, $S^*_{LII}(z)$ increases and quickly reaches a stable range of values at HAB $\simeq 30$ mm. For HAB > 30 mm, a nearly uniform $S^*_{LII}(z)$ is observed spatially. To our knowledge, this is the first time that the 2-D spatial evolution of the normalized LII signal from TiO_2 nanoparticles has been visualized in a flame.

Supposing that $R(\lambda, z)$ is spatially constant, the LII signal can be directly interpreted as $f^*_{\mathrm{v}}(z)$, according to Eq. (5). Such an assumption is often retained when using LII to investigate sooting particles [33, 34]. For the present case, its validity along the flame centerline has been verified in Fig. 8. Thus, $S^*_{LII}(z)$ signal in Fig. 9 provides a quite reasonable estimation of the spatial distribution of f^*_{v} for TiO_2 nanoparticles generated in the flame.

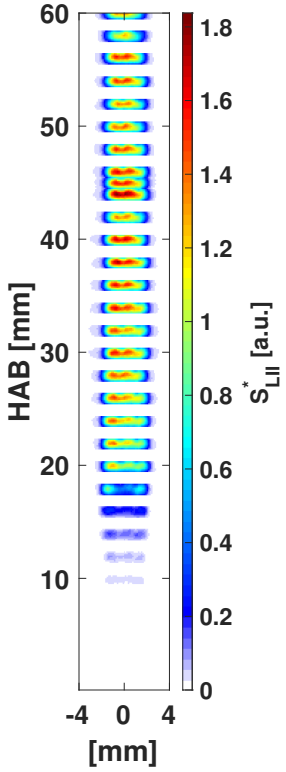

Figure 9: Spatial distribution of the normalized LII signal $S^*_{LII}(z)$ from TiO_2 nanoparticles generated in a laminar diffusion flame of argon-diluted hydrogen. Assuming a spatially constant $R(\lambda, z)$, it corresponds to the spatial distribution of the normalized volume fraction f^*_v of TiO_2.

3.2. LII decay time

The temporal decay of the LII signal contains information on the primary particle diameter [35]. The LII signal decay is linked to the decay of the particle temperature during its cooling process. In general, when the particles are heated at the same peak temperature, the LII decay rate can be linked to the primary particle size by assuming spherical particles: the smaller the particle, the quicker it will cool down and the shorter the LII signal is. Such direct relation is not straightforward when considering agglomerates and aggregates. For non-spherical particles, it is possible to define an equivalent sphere diameter based on a fractal-like approach. This definition accounts for the shielding effect, i.e., the more particles being inner part of the equivalent

sphere, the slower they will cool down since they are "thermally" shielded by the outer particles from cold ambient gas molecules [36, 37]. Thus, the LII signal can depend on the fractal dimension D_f, which is a parameter to characterize the morphology of aggregates/agglomerates. $D_f = 3$ denotes compact spherical geometry, while $D_f = 1$ corresponds to an open string shape. Thus, particle morphology can affect the LII signal decay [36, 37] so that attention has to be paid to interpreting τ in terms of the size of generated particles in flame.

Concerning TiO_2 nanoparticles in flame synthesis, previous works from Cignoli et al. [8] proved that the τ evolution is proportional to the particle count mean diameter measured by TEM. It is however impossible to quantitatively interpret τ in terms of primary particle size without additional information on the morphology of the particles in question. For this, ex-situ measurements, which are out-of-the scope of this work, will be required.

Still, information of τ can be used here to provide an indication of the evolution of the particle size. Figure 10(a) illustrates the normalized temporal evolution of LII measurement via PMT at 640 nm along the flame centerline for various flame heights (laser fluence of F=0.15 J/cm^2). We observe that the LII decay rate increases with the HABs.

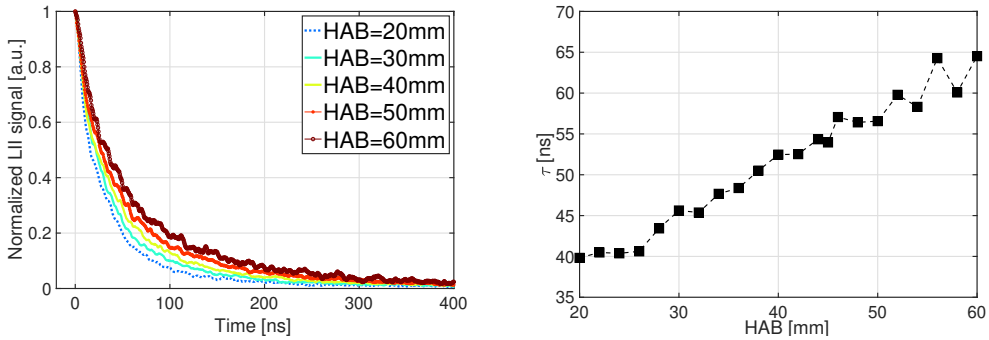

(a) (b)

Figure 10: (a)Normalized temporal evolution of the LII signal at 640 nm with a fluence of $F = 0.15$ J/cm^2 at various heights along the centerline. Each curve is normalized by its maximum value. (b) Evolution of the characteristic decay time τ along the flame centerline.

To illustrate this more clearly, the characteristic decay time:

$$\tau = \frac{t_i - t_j}{\ln(S_{\mathrm{LII}}(t_j)) - \ln(S_{\mathrm{LII}}(t_i))} \tag{6}$$

can be estimated from the S_{LII} signal at two instants t_i and t_j. Here, this quantity is calculated by considering the PMT measurements at prompt and with a delay of 100 ns from prompt. Results for τ along the flame centerline are presented in Fig. 10(b). The decay time does not increase significantly for HAB $<$ 26 mm. Then, it increases almost linearly with HAB.

The 2D field of the decay time can be obtained by considering the spatial information on the LII signal obtained with the camera at prompt and at delay time τ =100 ns. The spatial distribution of τ is shown in Fig. 12. As discussed in Fig. 10(b), along the flame centerline, a relatively stable value of τ is attained for HAB $\leq$ 26 mm. Subsequently, τ increases up to a factor of 2. Similar to S^*_{LII} results in Fig. 9, an almost homogeneous distribution is found for τ along the radial direction when looking at the 2D field of Fig. 12. Since only small variations of τ are found in the radial direction, it is likely that for a given HAB the particle size and morphology are not changing along the radial direction.

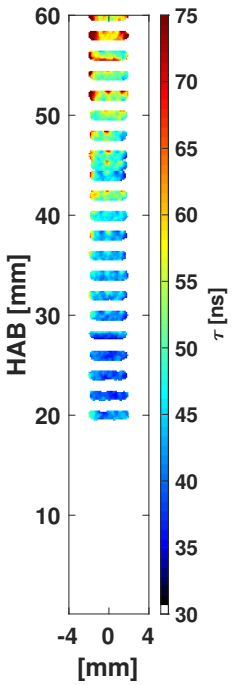

Figure 11

Figure 12: Spatial distribution of decay time of LII signal.

3.3. Discussion on the aerosol processes along the flame centerline

Along the flame centerline, it has been verified that $R(\lambda, z)$ is constant. Thus, it is possible to interpret the S^*_{LII} signal in terms of f^*_{v}. These results can be used together with results on τ to provide an insight into the aerosol process.

The f^*_{v} and τ evolution along the centerline are presented in Fig. 13. In this study, two distinct zones have been identified based on the HAB:

1. Zone I (HAB $\leq$ 26 mm): The normalized volume fraction f^*_{v} increases while τ only slightly varies, eventually indicating minor variations on particle size and morphology. This observation suggests that the nucleation process, i.e., the formation of nuclei, is the main contributor process at this stage. Mass growth mechanisms [38, 39], such as condensation or chemical surface growth, are likely to be negligible since τ is almost constant.

2. Zone II (HAB between 28-50 mm): The normalized volume fraction f_v^* reaches a plateau beyond HAB = 30 mm, whereas the decay time increases with HAB. The plateau in the volume fraction indicates no increase in mass, implying a small effect of nucleation, condensation, and surface growth in this zone. On the other hand, the increase in τ can be attributed to coalescence (merging of two or more particles into one so as to remove all boundaries between them), sintering (bonding and coalescence of particles into a larger cohesive structure at high temperature by mass-transport mechanisms), and/or agglomeration (process by which colliding particles adhere through the van der Waals force to form larger structures but with unchanged constituent particles [40]).

No conclusion of main processes occurring for HAB > 50mm can be provided with confidence since the flame fluctuation complicates the shot averaging in the measurements for high HABs. To the best of our knowledge, this is the first time that insight into the aerosol process for TiO_2 nanoparticles is provided with LII measurements in laminar coflow diffusion flames.

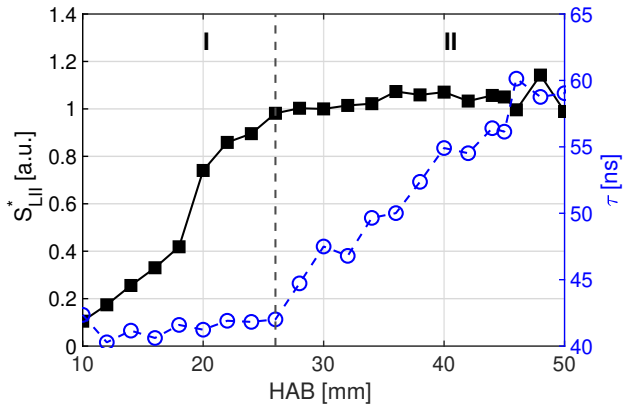

Figure 13: Evolution of normalized volume fraction and LII decay time along the flame height.

4. Conclusion

This study has presented the first steps toward the interpretation of the LII signal from flame-synthesized TiO_2 particles in terms of normalized volume fraction. For this, spectral, spatial, and temporal information were measured. The optimal conditions to perform LII for flame-synthesized TiO_2

have been identified through spectral measurement of LIE. The laser-induced emission spectra exhibit distinctive features depending on the fluence. The absence of carbon in the produced nanoparticles is inferred by comparing the spectral data obtained from the LIEs at a high fluence of flame-synthesized TiO_2 with reference spectra for carbon black and high-purity TiO_2 particles. LII signals at F= 0.15 J/cm^2 measured by a spatial detection system are then used to estimate the spatial evolution of the normalized TiO_2 volume fraction in the flame synthesis. By combining the temporal evolution of the LII signal with its spatial distribution, a first insight into the particle aerosol formation process along the flame centerline has been provided.

In the future, it is crucial to determine the spatial distribution of the absorption function needed to calibrate the LII signal [41]. To interpret the LII decay time in terms of primary particle size, complementary ex-situ measurements such as Transmission Electron Microscopy (TEM) or Scanning Mobility Particle Sizer (SMPS) are needed. Finally, it is essential to carefully investigate how the physical properties of particles change during the whole LII process since TiO_2 particles are characterized by quite a low melting temperature (T_{melting}=2150 K [42]). These results will improve our understanding of the production of flame-synthesized TiO_2 and provide an experimental database for the validation of the numerical strategies.

Acknowledgments

The authors acknowledge the support of the European Research Council (ERC) under the European Union's Horizon 2020 research and innovation program (grant agreement No. 757912).

Appendix A. Consistency between detection devices

To ensure that all three detection devices are consistent in terms of spectral, temporal, and spatial characteristics, the normalized temporal evolution of the signal at 640 ± 10 nm (or ± 7 nm for spatial detection) obtained by the three detection systems can be compared. Results at HAB = 30 mm in the flame centerline at various time delays are considered for a laser fluence of F= 0.15 J/cm^2. The spectral signals have been integrated over the target wavelength range. For spatial detection, the signal intensities for all pixels in the equivalent detection volume have been added up. The obtained quantities are visualized in Fig. A.14 as a function of the detection time delay and

are compared to the PMT signal. The three signals have been normalized at prompt. Overall, the normalized signals show good agreement between all three detection devices, which guarantees consistency between all three measurement systems.

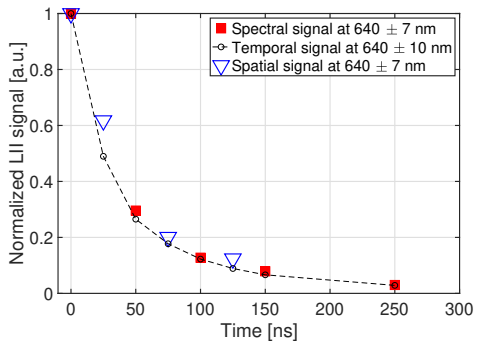

Figure A.14: Comparison between data from the three different detection devices for λ_{em} = 640 nm: ICCD camera on the spectrometer (spectral, red square symbol), PMT on the spectrometer (temporal, black round symbol with dashed line) and another ICCD camera (spatial, blue triangle symbol). Measurements were performed at HAB=30 mm in the flame centerline for $F = 0.15$ J/cm^2.

Appendix B. Repeatability

The repeatability of the LII measurement is examined here by looking at the evolution of PMT peak voltage along the flame centerline. The measurement campaign for PMT was repeated 7 times. Results are illustrated in Fig. B.15. The average data are represented by the continuous line, whereas the blue area indicates the standard deviation. The LII measurement data show about 30 % of standard deviation variation. This is probably due to TiO_2 production not being perfectly steady in the flame. This indicates a need for improvement in the experimental burner, particularly the injection system in the future. Still, the intensity, the spatial, and the temporal evolution of the signal are reproducible enough to allow for quantitative analysis of the normalized f_{v} and LII decay time of TiO_2 particles in the flame.

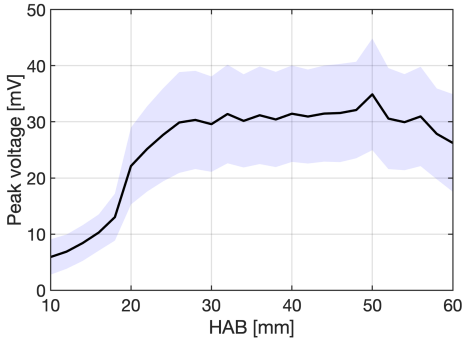

Figure B.15: Dispersion of LII signal intensity from 7 sets of temporal measurements via PMT at prompt along the flame centerline. Standard deviations (σ) are represented by blue area and the averaged values are represented in black lines.

References

[1] W. Y. Teoh, R. Amal, L. Mädler, Flame spray pyrolysis: An enabling technology for nanoparticles design and fabrication, Nanoscale 2 (8) (2010) 1324–1347.

[2] T. Dreier, C. Schulz, Laser-based diagnostics in the gas-phase synthesis of inorganic nanoparticles, Powder Technology 287 (2016) 226–238.

[3] Y. Ren, Y. Zhang, S. Li, Simultaneous single-shot two-dimensional imaging of nanoparticles and radicals in turbulent reactive flows, Physical Review Applied 13 (4) (2020) 044002.

[4] B. Franzelli, P. Scouflaire, N. Darabiha, Using in situ measurements to experimentally characterize tio2 nanoparticle synthesis in a turbulent isopropyl alcohol flame, Materials 14 (22) (2021) 7083.

[5] H. Michelsen, C. Schulz, G. Smallwood, S. Will, Laser-induced incandescence: Particulate diagnostics for combustion, atmospheric, and industrial applications, Progress in Energy and Combustion Science 51 (2015) 2–48.

[6] T. A. Sipkens, J. Menser, T. Dreier, C. Schulz, G. J. Smallwood, K. J. Daun, Laser-induced incandescence for non-soot nanoparticles: recent trends and current challenges, Applied Physics B 128 (4) (2022) 1–31.

[7] S. Maffi, F. Cignoli, C. Bellomunno, S. De Iuliis, G. Zizak, Spectral effects in laser induced incandescence application to flame-made titania nanoparticles, Spectrochimica Acta Part B: Atomic Spectroscopy 63 (2) (2008) 202–209.

[8] F. Cignoli, C. Bellomunno, S. Maffi, G. Zizak, Laser-induced incandescence of titania nanoparticles synthesized in a flame, Applied Physics B 96 (4) (2009) 593–599.

[9] S. De Iuliis, F. Migliorini, R. Dondè, Laser-induced emission of TiO_2 nanoparticles in flame spray synthesis, Applied Physics B 125 (11) (2019) 1–11.

[10] S. De Iuliis, R. Dondè, I. Altman, Light emission of flame-generated TiO_2 nanoparticles: Effect of ir laser irradiation, Journal of Quantitative Spectroscopy and Radiative Transfer 258 (2021) 107353.

[11] J. Yi, C. Betrancourt, N. Darabiha, B. Franzelli, Characterization of laser-induced emission of high-purity TiO_2 nanoparticles: feasibility of laser-induced incandescence, Applied Physics B 129 (6) (2023) 1–19.

[12] G. Xiong, S. Li, D. T. Stephen, Tuning excitation laser wavelength for secondary resonance in low-intensity phase-selective laser-induced breakdown spectroscopy for in-situ analytical measurement of nanoaerosols, Spectrochimica Acta Part B: Atomic Spectroscopy 140 (2018) 13–21.

[13] G. Jellison Jr, L. Boatner, J. Budai, B.-S. Jeong, D. Norton, Spectroscopic ellipsometry of thin film and bulk anatase (TiO_2), Journal of Applied Physics 93 (12) (2003) 9537–9541.

[14] H.-Y. Liu, Y.-L. Hsu, H.-Y. Su, R.-C. Huang, F.-Y. Hou, G.-C. Tu, W.-H. Liu, A comparative study of amorphous, anatase, rutile, and mixed phase TiO_2 films by mist chemical vapor deposition and ultraviolet photodetectors applications, IEEE Sensors Journal 18 (10) (2018) 4022–4029.

[15] Sooting yale coflow diffusion flames, available at http://guilford.eng.yale.edu/yalecoflowflames/ (2016).

[16] J. Menser, K. Daun, T. Dreier, C. Schulz, Laser-induced atomic emission of silicon nanoparticles during laser-induced heating, Applied optics 56 (11) (2017) E50–E57.

[17] J. Menser, K. Daun, C. Schulz, Interrogating gas-borne nanoparticles using laser-based diagnostics and bayesian data fusion, The Journal of Physical Chemistry C 125 (15) (2021) 8382–8390.

[18] K. Daun, J. Menser, R. Mansmann, S. T. Moghaddam, T. Dreier, C. Schulz, Spectroscopic models for laser-heated silicon and copper nanoparticles, Journal of Quantitative Spectroscopy and Radiative Transfer 197 (2017) 3–11.

[19] M. A. Green, Self-consistent optical parameters of intrinsic silicon at 300 k including temperature coefficients, Solar Energy Materials and Solar Cells 92 (11) (2008) 1305–1310.

[20] K. Shvarev, B. Baum, P. Gel'd, Optical properties and electronic characteristics of liquid solutions of nickel in silicon, Soviet Physics Journal 18 (4) (1975) 521–524.

[21] S. Talebi-Moghaddam, T. Sipkens, K. Daun, Laser-induced incandescence on metal nanoparticles: validity of the rayleigh approximation, Applied Physics B 125 (2019) 1–16.

[22] G. De Falco, M. Commodo, P. Minutolo, A. D'Anna, Flame aerosol synthesis and thermophoretic deposition of superhydrophilic TiO_2 nanoparticle coatings, Chemical Engineering Transactions 73 (2019) 37–42.

[23] A. Kramida, Yu. Ralchenko, J. Reader, and NIST ASD Team, NIST Atomic Spectra Database (ver. 5.9), [Online]. Available: `https://physics.nist.gov/asd` [2022, June 2]. National Institute of Standards and Technology, Gaithersburg, MD. (2021).

[24] Y. Ren, K. Ran, S. Kruse, J. Mayer, H. Pitsch, Flame synthesis of carbon metal-oxide nanocomposites in a counterflow burner, Proceedings of the Combustion Institute 38 (1) (2021) 1269–1277.

[25] F. Goulay, L. Nemes, P. E. Schrader, H. A. Michelsen, Spontaneous emission from C_2 ($d^3\Pi_g$) and C_3 ($A\ ^1\Pi_u$) during laser irradiation of soot particles, Molecular Physics 108 (7-9) (2010) 1013–1025.

[26] N. K. Memon, D. H. Anjum, S. H. Chung, Multiple-diffusion flame synthesis of pure anatase and carbon-coated titanium dioxide nanoparticles, Combustion and flame 160 (9) (2013) 1848–1856.

[27] R. A. Dobbins, C. M. Megaridis, Absorption and scattering of light by polydisperse aggregates, Applied optics 30 (33) (1991) 4747–4754.

[28] J.-P. Jalava, V.-M. Taavitsainen, R.-J. Lamminmäki, M. Lindholm, S. Auvinen, M. Alatalo, E. Vartiainen, H. Haario, Modeling tio2 s refractive index function from bulk to nanoparticles, Journal of Quantitative Spectroscopy and Radiative Transfer 167 (2015) 105–118.

[29] D. R. Snelling, G. J. Smallwood, F. Liu, Ö. L. Gülder, W. D. Bachalo, A calibration-independent laser-induced incandescence technique for soot measurement by detecting absolute light intensity, Applied optics 44 (31) (2005) 6773–6785.

[30] T. Siefke, S. Kroker, K. Pfeiffer, O. Puffky, K. Dietrich, D. Franta, I. Ohlídal, A. Szeghalmi, E.-B. Kley, A. Tünnermann, Materials pushing the application limits of wire grid polarizers further into the deep ultraviolet spectral range, Advanced Optical Materials 4 (11) (2016) 1780–1786.

[31] S. Sarkar, V. Gupta, M. Kumar, J. Schubert, P. T. Probst, J. Joseph, T. A. König, Hybridized guided-mode resonances via colloidal plasmonic self-assembled grating, ACS applied materials & interfaces 11 (14) (2019) 13752–13760.

[32] M. Planck, The theory of heat radiation, Entropie 144 (190) (1900) 164.

[33] A. Coderre, K. Thomson, D. Snelling, M. Johnson, Spectrally resolved light absorption properties of cooled soot from a methane flame, Applied Physics B 104 (2011) 175–188.

[34] M. Köhler, K. P. Geigle, W. Meier, B. M. Crosland, K. A. Thomson, G. J. Smallwood, Sooting turbulent jet flame: characterization and quantitative soot measurements, Applied Physics B 104 (2011) 409–425.

[35] S. Will, S. Schraml, A. Leipert, Comprehensive two-dimensional soot diagnostics based on laser-induced incandescence (LII), in: Symposium (International) on Combustion, Vol. 26, Elsevier, 1996, pp. 2277–2284.

[36] F. Liu, M. Yang, F. A. Hill, D. R. Snelling, G. J. Smallwood, Influence of polydisperse distributions of both primary particle and aggregate size on soot temperature in low-fluence LII, Applied Physics B 83 (3) (2006) 383.

[37] H. Bladh, J. Johnsson, J. Rissler, H. Abdulhamid, N.-E. Olofsson, M. Sanati, J. Pagels, P.-E. Bengtsson, Influence of soot particle aggregation on time-resolved laser-induced incandescence signals, Applied Physics B 104 (2) (2011) 331–341.

[38] C. Weise, J. Menser, S. Kaiser, A. Kempf, I. Wlokas, Numerical investigation of the process steps in a spray flame reactor for nanoparticle synthesis, Proceedings of the Combustion Institute 35 (2) (2015) 2259–2266.

[39] Y. Wang, P. Liu, J. Fang, W.-N. Wang, P. Biswas, Kinetics of sub-2 nm tio 2 particle formation in an aerosol reactor during thermal decomposition of titanium tetraisopropoxide, Journal of Nanoparticle Research 17 (2015) 1–13.

[40] V. Raman, R. O. Fox, Modeling of fine-particle formation in turbulent flames, Annual Review of Fluid Mechanics 48 (2016) 159–190.

[41] F. Migliorini, K. Thomson, G. Smallwood, Investigation of optical properties of aging soot, Applied Physics B 104 (2011) 273–283.

[42] D. R. Collins, W. Smith, N. M. Harrison, T. R. Forester, Molecular dynamics study of tio2 microclusters, Journal of Materials Chemistry 6 (8) (1996) 1385–1390.